

## **A SEQUENTIAL IMPLICIT ALGORITHM OF CHEMO-THERMO-PORO-MECHANICS FOR FRACTURED GEOTHERMAL RESERVOIRS**

Jihoon Kim, Eric Sonnenthal, Jonny Rutqvist

Lawrence Berkeley National Laboratory  
1 Cyclotron Rd.  
Berkeley CA, 94720, USA  
e-mail: JihoonKim@lbl.gov

### **ABSTRACT**

Here we describe the development of a sequential implicit formulation and algorithm for coupling fluid-heat flow, reactive transport, and geomechanics. We consider changes in pore volume from dissolution and precipitation caused by chemical reactions, in addition to coupled flow and geomechanics. Moreover, we use the constitutive equations for a multiple porosity model for fractured geothermal reservoirs, employing nonlinear permeability and Young's modulus for the fractures and dynamically updating them every time step. For a well-defined simple test problem, we explore the differences in coupled flow and geomechanics with and without reactive transport.

### **1. INTRODUCTION**

Enhanced geothermal reservoirs that exhibit increased permeability resulting from shear stimulation of a fracture volume can provide large heat extraction accompanied by economic flow rates and energy production. Fractures are highly compressible compared with intact rock, so they may affect overall geomechanical responses significantly, even though they occupy a smaller bulk volume. Permeability can be significantly affected by deformation of fractures through the relationship between fracture aperture and permeability. Furthermore, chemical or thermal disequilibrium between injection fluid and the reservoir host rock can result in dissolution and precipitation, changing the porosity. Such changes in pore volume can change fluid pressure, and hence effective stress and strain. Permeability changes through mineral-water reactions and geomechanics affects solute transport which can lead to strong thermal, hydrological, mechanical, and chemical coupling.

The multiple continuum approach is a widely used approach that can represent fracture-rock matrix systems consisting of highly permeable fracture continuum transporting fluid over the domain, while the matrix store fluid and convey it to the highly permeable fracture continuum (Barenblatt et al., 1960; Berryman, 2002; Sonnenthal et al., 2005; Taron et al., 2009). In geothermal reservoirs, we may introduce more than two continua (e.g., representing fracture and several rock matrix continua) for more accurate modeling of heat flow. Recently, Kim et al. (2012) proposed formulation and sequential numerical algorithms for coupled fluid-heat flow and geomechanics within such a multiple continuum approach.

This study is based on the latter study, and employing nonlinear dynamic strain-dependent permeability and geomechanical moduli in order to capture complex interactions between flow and geomechanics, as applied to shale gas reservoirs (Kim and Moridis, 2012b). Moreover, we consider the changes in pore volume, induced by chemical reaction, when solving for fluid and heat flow.

We have recently implemented these functionalities within ROCMECH (RM for short), an in-house geomechanics simulator, which is coupled to TOUGHREACT (TR), a flow and reactive transport simulator (Kim et al., 2012). We solve fluid and heat flow, geomechanics, and reactive transport problems sequentially, adopting implicit solution schemes for the subproblems (i.e., sequential implicit method). Based on the coupled simulator, TR-RM, flow-geomechanics properties and variables (e.g., porosity, permeability, fluid-phase pressure and saturation, displacement, effective stress, geomechanical moduli, failure

status) are updated dynamically along with the transient coupled simulation.

We performed several verification test cases for TR-RM (e.g., the Terzaghi and Mandel problems), as well as a 1D reactive transport problem. Then, we investigated a 2D geothermal problem, using coupled thermo-poro-mechanics simulations with and without reactive transport, and analyze the differences between them in the results.

## 2. MATHEMATICAL FORMULATION

We briefly describe the governing equations of geomechanics, fluid and heat flow with reactive solute transport. Then, we introduce constitutive equations for the multiple porosity model, the changes in pore volume from chemical reactions, nonlinear permeability, and Young's modulus.

### 2.1. Governing Equation

The governing equation for geomechanics is based on the quasi-static assumption, written as

$$\mathbf{Div}\boldsymbol{\sigma} + \rho_b \mathbf{g} = \mathbf{0}, \quad (1)$$

where  $\mathbf{Div}$  is the divergence operator,  $\boldsymbol{\sigma}$  is the total stress tensor, and  $\rho_b$  is the bulk density. An infinitesimal transformation is used to allow the strain tensor,  $\boldsymbol{\varepsilon}$ , to be the symmetric gradient of the displacement vector,  $\mathbf{u}$ ,

$$\boldsymbol{\varepsilon} = \frac{1}{2} (\mathbf{Grad}^T \mathbf{u} + \mathbf{Grad} \mathbf{u}) \quad (2)$$

where  $\mathbf{Grad}$  is the gradient operator.

The governing equations for fluid and heat flow are derived from the conservation law (Pruess et al., 1999), as follows,

$$\frac{d}{dt} \int_{\Omega} m^k d\Omega + \int_{\Gamma} \mathbf{f}^k \cdot \mathbf{n} d\Gamma - = \int_{\Omega} q^k d\Omega \quad (3)$$

where the superscript  $k$  indicates the fluid components or heat.  $d(\cdot)/dt$  denotes the time derivative of a physical quantity  $(\cdot)$  relative to the motion of the solid skeleton.  $m^k$  is the mass of component  $k$  or heat.  $\mathbf{f}^k$ , and  $q^k$  are its flux

and source terms on the domain  $\Omega$  with the boundary  $\Gamma$ , respectively, where  $\mathbf{n}$  is the normal vector of the boundary.

The flux for multiphase multicomponent flow is supplemented by Darcy's and Fick's laws. The heat flux is obtained by heat conduction and convection laws. The governing equation for solute transport with reactive transport is obtained from mass conservation (Xu et al., 2011), described as

$$\begin{aligned} & \frac{d}{dt} (\Phi C_i) + \mathbf{Div}(\Phi \mathbf{v}_i C_i - \Phi \mathbf{D}_i \mathbf{Grad} C_i) \\ & = - \sum_{m=1}^{n_c} \gamma_{im} r_m + q_i, \end{aligned} \quad (4)$$

where Lagrange's porosity,  $\Phi$ , is defined as the ratio of the pore volume in the deformed configuration to the bulk volume in the reference (initial) configuration.  $C_i$  is the concentration of the  $i^{\text{th}}$  chemical.  $\mathbf{v}_i$  and  $\mathbf{D}_i$  are the Darcy velocity vector and diffusion coefficient of the  $i^{\text{th}}$  chemical, respectively.  $\gamma_{im}$  and  $r_m$  are the stoichiometric coefficient of the  $i^{\text{th}}$  chemical in the  $m^{\text{th}}$  chemical and the reaction rate of the  $m^{\text{th}}$  chemical, respectively.  $n_c$  is the total number of the chemicals, and  $q_i$  is the possible external source of the  $i^{\text{th}}$  chemical.

### 2.2. Constitutive relations

We employ the constitutive equations proposed by Kim et al. (2012) for the multiple porosity model, extended from the isothermal double porosity elastic model (Berryman, 2002) to the nonisothermal multiple porosity elastoplastic model, described as

$$\delta \boldsymbol{\sigma} = \overbrace{\mathbf{C}_{up}^{\delta \boldsymbol{\sigma}'}}_{\delta \boldsymbol{\sigma}'} - \sum_{l,j} b_{l,j}^* \delta p_{l,j} \mathbf{1} - \sum_l \tilde{b}_l^* \delta T_l \mathbf{1}, \quad (5)$$

$$\begin{aligned} b_{l,j}^* &= -K_{dr} b_l S_{l,j}, \quad \tilde{b}_l^* = -K_{dr} \tilde{b}_l, \\ \delta \xi_{l,j} &= b_{l,j}^* \delta \varepsilon_v + \sum_{m,l} L_{l,j,m,l}^{-1} \delta p_{m,l} \\ &+ \sum_{m,l} \bar{D}_{lm} \delta T_m, \end{aligned} \quad (6)$$

where the subscript  $l$  indicates a material (sub-element) with a gridblock.  $\boldsymbol{\sigma}'$ ,  $K_{dr}$ ,  $\mathbf{C}_{up}$  are the effective stress tensor, upscaled drained bulk

modulus, and upscaled elasticity tensor at the level of the gridblock, respectively.  $\delta \xi_{l,j} = \delta m_{l,j} / \rho_{l,j} \cdot b_{l,j}^*$  and  $\tilde{b}_l^*$  are the coupling coefficients, where  $b_l$  and  $\tilde{b}_l$  are written as

$$b_l = -\frac{\alpha_l \eta_l}{K_l}, \tilde{b}_l = -3\alpha_{T,l} \eta_l, \alpha_l = 1 - \frac{K_l}{K_s}, \quad (7)$$

where  $\alpha_l$ ,  $\alpha_{T,l}$ ,  $\eta_l$ , and  $K_l$  are the Biot coefficient, thermal dilation coefficient, volume fraction, and drained bulk modulus for material  $l$ , respectively.  $K_s$  is the intrinsic solid grain bulk modulus.  $K_{dr}$  and  $\mathbf{C}_{up}$  are described as

$$K_{dr} = \sum_{l=1}^{n_m} \frac{\eta_l}{K_l}, \mathbf{C}_{up} = K_{dr} \sum_{l=1}^{n_m} \frac{\eta_l}{K_l} \mathbf{C}_l, \quad (8)$$

where  $\mathbf{C}_l$  is the isothermal drained elasticity tensor for material  $l$ .  $n_m$  is the total number of the materials.  $L_{l,j,m,l}$  represents a modulus for the multiple porous model, similar to the Biot modulus matrix, and the inverse of its matrix form (i.e.,  $\mathbf{L}^{-1}$ ) can be expressed as an example of an vapor-water two-phase system with the fracture-rock matrix double porosity model,

$$\mathbf{L}^{-1} = \begin{bmatrix} \eta_f \mathbf{N}_f & \mathbf{0} \\ \mathbf{0} & \eta_M \mathbf{N}_M \end{bmatrix}, \quad (9)$$

where  $\mathbf{N}_f$  and  $\mathbf{N}_M$  are the inverse of the Biot modulus matrices,  $\mathbf{M}_f$  and  $\mathbf{M}_M$ , for the fracture and rock matrix, respectively.  $\bar{D}_{lm}$  is the coupling coefficient between fluid flow and heat flow.

The effective stress at each subelement  $l$ ,  $\boldsymbol{\sigma}_l'$ , is obtained as

$$\delta \boldsymbol{\sigma}' = \sum_l \eta_l \delta \boldsymbol{\sigma}_l', \delta \boldsymbol{\sigma}_l' = \mathbf{C}_l \delta \boldsymbol{\varepsilon}_l, \delta \boldsymbol{\varepsilon}_l = \frac{K_{dr}}{K_l} \delta \boldsymbol{\varepsilon}, \quad (10)$$

where  $\boldsymbol{\varepsilon}_l$  is the local total strain at each subelement  $l$ . According to Kim et al. (2012), Lagrange's porosity of material  $l$  without chemical reaction,  $\Phi_l^M$ , can be written as

$$\delta \Phi_l^M = \left( \frac{\alpha_l^2}{K_l} + \frac{\alpha_l - \Phi_l}{K_s} \right) \delta p_l + 3\alpha_{T,l} \alpha_l \delta T_l - \frac{b_l}{\eta_l} \delta \sigma_v, \quad (11)$$

where  $\sigma_v$  is the total volumetric mean stress. Equation 11 is typically known as the porosity change, when reservoir simulation is coupled to geomechanics. The additional change in the porosity due to reactive solute transport can be formulated as (Xu et al., 2006)

$$\delta \Phi_l^C = -\sum_{m=1}^{n_c} \delta \chi_{m,l}, \quad (12)$$

where  $\chi_{m,l}$  is the  $m^{\text{th}}$  solid volume fraction of material  $l$ . Then, from Equations (11) and (12), we obtain the total porosity change due to geomechanics and geochemistry, as follows.

$$\begin{aligned} \delta \Phi_l &= \delta \Phi_l^M + \delta \Phi_l^C \\ &= \left( \frac{\alpha_l^2}{K_l} + \frac{\alpha_l - \Phi_l}{K_s} \right) \delta p_l + 3\alpha_{T,l} \alpha_l \delta T_l \\ &\quad - \frac{b_l}{\eta_l} \delta \sigma_v - \sum_{m=1}^{n_c} \delta \chi_{m,l} \end{aligned} \quad (13)$$

For permeability and stiffness of the fractured medium, we employ the strain-dependent permeability and Young's modulus. For an example of 2D plane strain geomechanics coupled to fluid flow, as used in Kim and Moridis (2012b), we use in this study

$$k_{xx}^p = k_{xx,0}^p (1 + \varepsilon_{xx})^3, k_{zz}^p = k_{zz,0}^p (1 + \varepsilon_{zz})^3, \\ E_x = E_{x,0} \frac{1}{(1 + \varepsilon_{xx})^2}, E_z = E_{z,0} \frac{1}{(1 + \varepsilon_{zz})^2}, \quad (14)$$

where  $k^p$  and  $E$  are the absolute permeability and Young's modulus. We may use different types of the nonlinear permeability and Young's modulus for specific conditions or reservoirs.

For modeling elastoplastic shear failure, we use the Drucker-Prager and Mohr-Coulomb models, which are widely used to model failure in cohesive frictional materials. The Drucker-Prager model is expressed as

$$f = \beta_f I_1 + \sqrt{J_2} - \kappa_f \leq 0, \quad (15)$$

$$g = \beta_g I_1 + \sqrt{J_2} - \kappa_g \leq 0,$$

where  $I_1$  is the first invariant of the effective stress and  $J_2$  is the second stress invariant of the effective deviatoric stress. The Mohr-Coulomb model is given as

$$f = \tau'_m - \sigma'_m \sin \Psi_f - c_h \cos \Psi_f \leq 0, \quad (16)$$

$$g = \tau'_m - \sigma'_m \sin \Psi_d - c_h \cos \Psi_d \leq 0,$$

$$\sigma'_m = \frac{\sigma'_1 + \sigma'_3}{2}, \quad \tau'_m = \frac{\sigma'_1 - \sigma'_3}{2}, \quad (17)$$

where  $\sigma'_1$ ,  $\sigma'_2$ ,  $\sigma'_3$  are the maximum, intermediate, and minimum principal effective stresses.  $\Psi_f$  and  $\Psi_d$  are the friction and dilation angles, respectively.  $c_h$  is the cohesion.

### 3. NUMERICAL INTEGRATION

For space discretization, we use finite volume and finite element methods for flow and geomechanics, respectively. In time discretization, the backward method is used as typically employed in reservoir simulation. The initial total stress satisfies the geomechanical equilibrium with the boundary conditions. We implement in TR-RM the numerical modeling for the Mohr-Coulomb and Drucker-Prager models with slight modification of the algorithms proposed by Wang et al. (2004), which has been applied to the numerical studies in Kim et al. (2012a). TR-RM thus has the capability to simulate hydro-shearing (shear activation of fractures by hydraulic pressurization) as a continuum shear failure process.

In numerical integration, we use a sequential implicit approach, by which fluid and heat flow, geomechanics, and reactive solute transport are solved sequentially, with each subproblem being solved implicitly. We extend the modified fixed-stress-split method in coupling between fluid and heat flow and geomechanics for the multiple porosity model, to a chemo-thermo-poro-mechanics approach. Specifically, from Equation 13, we can easily implement the

extended and modified fixed stress split by using porosity function and correction, as follows.

$$\begin{aligned} \Delta \Phi_l^n = & \left( \frac{\alpha_l^2}{K_l^n} + \frac{\alpha_l - \Phi_l^n}{K_s} + \omega_p^c \right) \Delta p_l^n \\ & + \left( 3\alpha_{T,l} \alpha_l + \omega_T^c \right) \Delta T_l^n - \frac{b_l}{\eta_l} \Delta \sigma_v^{n-1} \\ & - \left( \omega_p^c \Delta p_l^{n-1} + \omega_T^c \Delta T_l^{n-1} - \Delta \Phi_l^{C,n-1} \right) \end{aligned} \quad (18)$$

where  $\Delta(\cdot)^n = (\cdot)^{n+1} - (\cdot)^n$ .  $\omega_p^c$  and  $\omega_T^c$  are introduced as relaxation parameters for numerical stabilization due to chemical reaction. Even though the modified fixed stress split for the multiple porosity model is unconditionally stable for thermo-poro-mechanics (Kim et al., 2012), it cannot guarantee unconditional stability of chemo-thermo-poro-mechanics, because thermo-poro-mechanics is a subproblem of chemo-thermo-poro-mechanics. (Determining  $\omega_p^c$  and  $\omega_T^c$  is an open question, which will not be discussed in this study.)

For permeability and Young's modulus of the fracture medium, we use the explicit treatment, as follows.

$$\begin{aligned} k_{xx}^{p,n+1} &= k_{xx,0}^p (1 + \varepsilon_{xx}^n)^3, \quad k_{zz}^{n+1} = k_{zz,0}^{n+1} (1 + \varepsilon_{zz}^n)^3 \\ E_x^{n+1} &= E_{x,0} \frac{1}{(1 + \varepsilon_{xx}^n)^2}, \quad E_z^{n+1} = E_{z,0} \frac{1}{(1 + \varepsilon_{zz}^n)^2}, \end{aligned} \quad (19)$$

### 4. NUMERICAL EXAMPLES

We first conduct verification tests for TR-RM's chemo-thermo-poro-mechanics approach. To this end, we first introduce the Terzaghi and Mandel problems to verify the simulator in poromechanics. Then we compare TR only with TR-RM in a 1D elastic single-phase flow problem, because the 1D elastic problem can allow the decoupling of flow and geomechanics, using an exact rock compressibility. After verification, we compare the numerical results among chemo-thermo-poro-mechanics, thermo-poro-mechanics without reactive transport, and TR-only with and without reactive transport.

#### 4.1. Terzaghi's and Mandel's problems

Figure 1 shows the domains for the Terzaghi and Mandel problems. For Terzaghi's problem, we have 31 gridblocks, the sizes of which are uniform, 1.0 m. Liquid water is fully saturated, and the initial pressure is 8.3 MPa. We impose a drainage boundary on the left side and no-flow conditions on the right side. The initial total stress is also 8.3 MPa over the domain, and we set 16.6 MPa as the side burden, two times greater than the initial total stress. The Young's modulus and Poisson ratio are 450 MPa and 0.0, respectively. Only horizontal displacement is allowed. The monitoring well is located at the right end.

For Mandel's problem, we have  $40 \times 5$  gridblocks. The size of the gridblocks in the x direction is uniform, 0.5 m, while the size in the z direction is non-uniform. The medium is fully saturated with water, and the initial pressure is 10.0 MPa. We impose drainage boundaries at the left and right sides, and no-flow conditions on the other sides. Initial total stress is also 10.0 MPa over the domain, and we set 20.0 MPa for the overburden, two times greater than the initial total stress. The Young's modulus and Poisson ratio are 450 MPa and 0.0, respectively. 2D plane strain geomechanics is employed. The monitoring well is located in the middle of the domain, as shown in Figure 1. No gravity is considered for the Terzaghi and Mandel problems. The permeability and porosity are  $6.51 \times 10^{-15} \text{ m}^2$ , 6.6 mD (1 Darcy =  $9.87 \times 10^{-13} \text{ m}^2$ ), and 0.425, respectively for both problems. Biot's coefficient is 1.0.

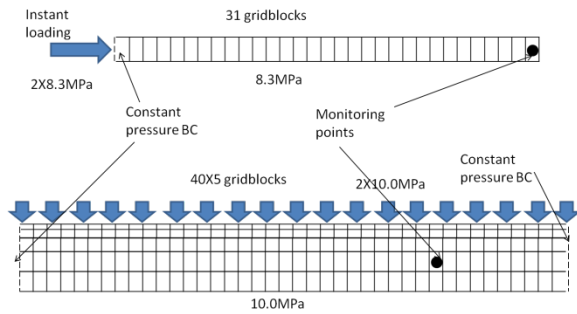


Figure 1. The domains for Terzaghi's (top) and Mandel's problems (bottom).

Figures 2 and 3 show that the results from TR-RM match the analytical solutions. The

numerical results correctly capture the instantaneous pressure buildup for Terzaghi's problem and the Mandel-Cryer effect for Mandel's problem—these could not be captured by a flow-only simulation.

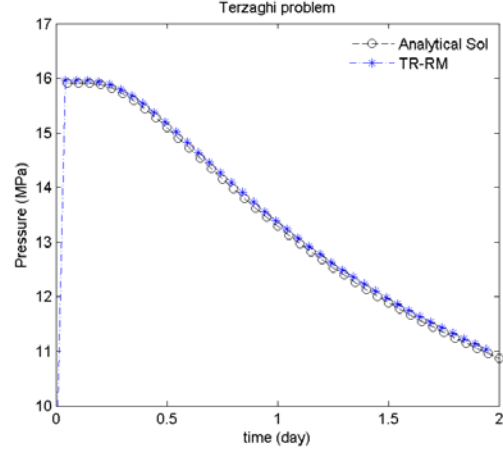


Figure 2. Comparison between the analytical solution and the result of TR-RM for Terzaghi's problem.

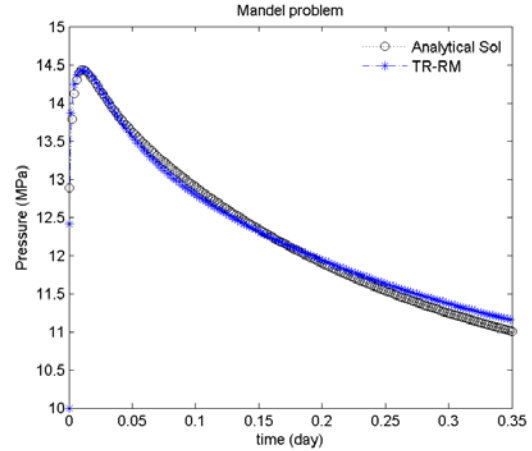


Figure 3. Comparison between the analytical solution and the result of TR-RM for Mandel's problem.

#### 4.2. 1D chemo-poro-mechanics

We reuse the domain, initial conditions, and geomechanics and flow properties of the Terzaghi problem. We have the same side burden of the initial pressure. The monitoring point is located at the third gridblock from the right end. Isothermal single-phase flow is considered. We employ  $\omega_p^c = -3.6 \times 10^{-9} \text{ Pa}^{-1}$  for numerical stability. The production and injection are applied to the left and right end gridblocks,

respectively with the same rate,  $1.0 \times 10^{-4}$  kg/s. Quartz dissolution was assumed to be the only reaction as observed in the experiment described by Johnson et al. (1998), and modeled using a linear kinetic rate law.

From Figure 4, we can see that the result of TR-RM matches the result for TR-only. At initial time, the pressure increases instantaneously due to the injection, and then drops rapidly due to chemical dissolution. Dissolution causes an increase in pore volume, which causes a decrease in pressure based on fluid compressibility. After the initial time, the pressure increases again, reaching steady state.

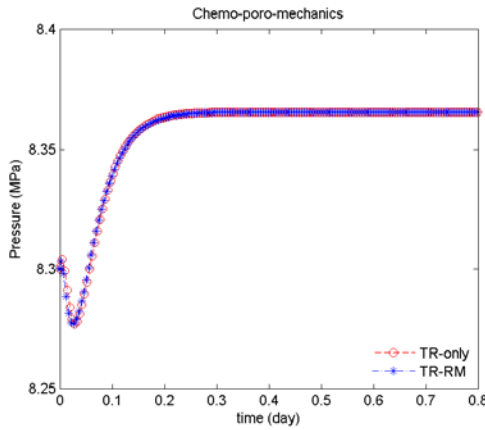


Figure 4. Comparison of the results between TR only and TR-RM for the 1D chemo-poro-mechanics problem.

#### 4.3. 2D chemo-thermo-poro-mechanics

We consider the fractured geothermal problem shown in Figure 5. The geothermal reservoir has a large dimension perpendicular to the fracture plane, i.e., the problem can be reduced to one of multiple porosity 2D plane strain geomechanics, as shown in Figure 6.

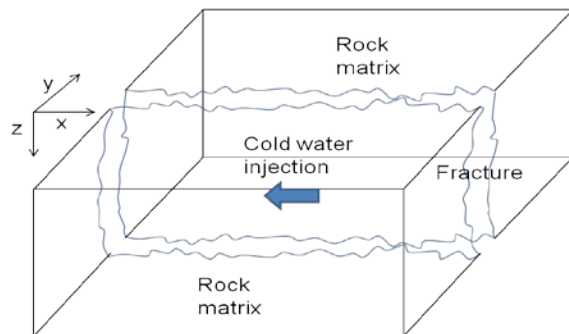


Figure 5. The schematics of a 3D fractured geothermal reservoir

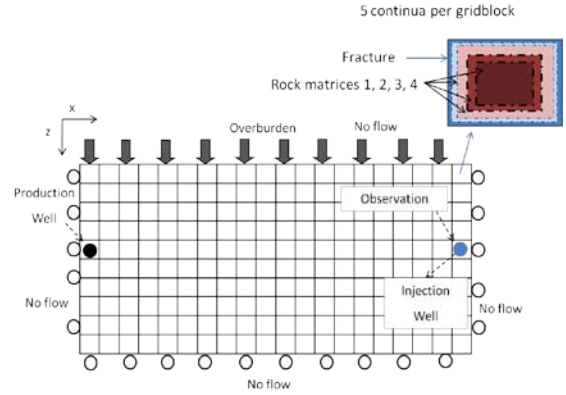


Figure 6. The discretized domain of the fractured geothermal reservoir with the 2D plane strain geomechanics and the multiple porosity model.

For the 2D problem, we have  $20 \times 10$  gridblocks in the x and z directions, the sizes of which are uniform, 10.0 m. The size of the dimension in the y direction is 500 m, large enough for the constant temperature boundary for heat flow. Each gridblock has five subelements, one fracture and four rock matrix domains, the volume fractions of which are 0.002, 0.098, 0.20, 0.35, and 0.35, respectively. The reservoir is fully water saturated, and the initial pressure and temperature at the top are 19.0 MPa and 146.7°C, respectively, which is much cooler than a producing geothermal system, but which shows qualitatively the same behavior. They are distributed with the hydrostatic pressure gradient, 9806 Pa/m, and the geothermal gradient, 25°C/km. The initial permeabilities of the fracture and the rock matrices are  $5.9 \times 10^{-13}$  m<sup>2</sup> and  $5.9 \times 10^{-19}$  m<sup>2</sup>, respectively, and their porosities are 0.5 and 0.3, respectively. We impose no-flow boundaries on all sides. Heat conductivities under desaturated and saturated conditions are 0.5 W/m°C and 3.1 W/m°C, respectively, for all the materials. Specific heat capacity is 1000 J/kg/°C for all materials. The monitoring point is the fracture medium at the injection point, as shown in Figure 6.

For geochemistry, we take the same quartz dissolution process used in the previous 1D chemo-poro-mechanics problem. For geomechanics, the initial vertical principal total stress is 19.0 MPa at the top, vertically distributed based on the bulk density, 2200 kg/m<sup>3</sup>.

The horizontal principal total stress in the x direction is the same as the vertical stress. We have 19.0 MPa overburden, and horizontally constrained boundaries at the sides and no vertical displacement at the bottom. Young's modulus and Poisson's ratio for the fracture are 213.75 MPa and 0.0, respectively. Young's modulus and Poisson's ratio for the rock matrices are 5.586 GPa and 0.0, respectively. We use  $\omega_p^c = 0.0 \text{ Pa}^{-1}$  and  $\omega_T^c = 0.0^\circ\text{C}^{-1}$ . Biot's coefficients and thermal dilation coefficients are 1.0 and  $4.5 \times 10^{-5} \text{ }^\circ\text{C}^{-1}$  for all materials. The injection and production wells are located on the right and left sides of the domain, as shown in Figure 6. Injection and production rates are 50.0 kg/s, with  $20^\circ\text{C}$  water and 50.0 kg/s with water of the reservoir temperature, respectively.

Figure 7 shows the comparison between chemo-thermo-poro-mechanics and thermo-poro-mechanics without reactive transport. Figure 8 also shows the comparison between TR only with and without reactive transport. In Figure 7, unlike with TR only, we observe the increase in pressure with TR-RM, resulting from the complicated interactions between the fracture and rock matrices due to mechanical and thermal contraction or dilation.

Comparing Figure 7 with Figure 8, we find that cold-water injection induces thermal contraction, followed by the support of the reservoir pressure, which can be properly captured by the coupling between flow and geomechanics.

In Figure 8, TR-only with geochemistry shows more pressure drop than TR-only without geochemistry, because the dissolution increases the pore volume, as shown in Figure 9, which causes the pressure drop. However, we observe that the pressure of chemo-thermo-poro-mechanics is slightly higher than the pressure of thermo-poro-mechanics. The monitoring point is affected by the compaction due to dissolution at another location, and undergoes additional compaction and decrease in porosity, unlike thermo-poro-mechanics without the reactive transport shown in Figure 9. Note that the perturbation of geomechanics at a certain location affects the entire domain

instantaneously, because of the nature of quasi-static mechanics.

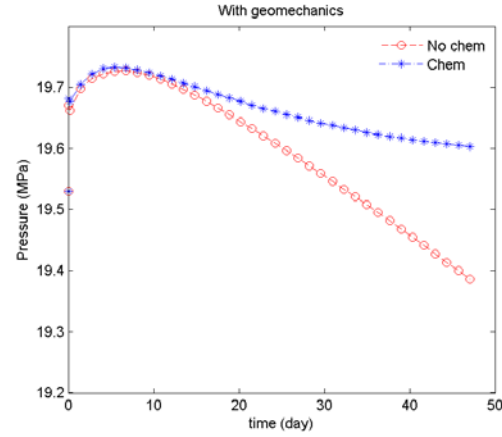


Figure 7. Comparison of the pressure results between chemo-thermo-poro-mechanics, ('Chem'), and thermo-poro-mechanics only, ('No chem').

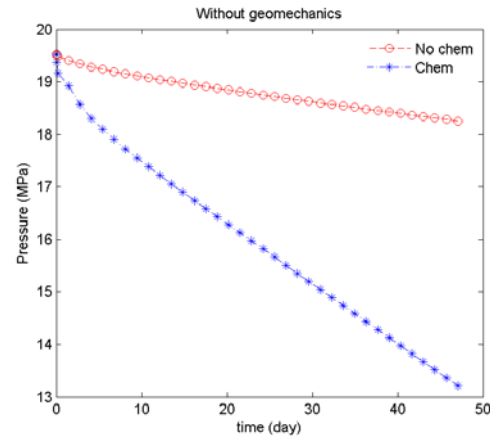


Figure 8. Comparison of the pressure results between with ('Chem') and without ('No chem') reactive transport in TR-only.

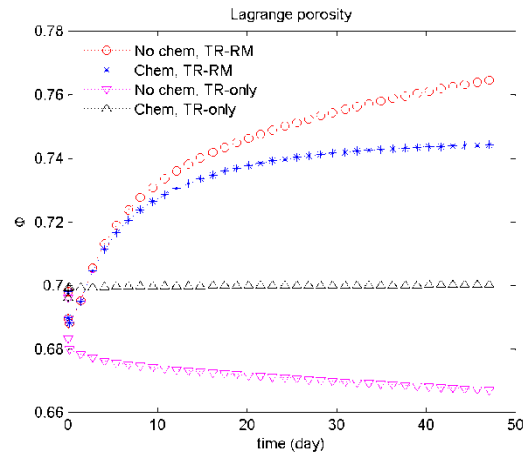


Figure 9. Comparison of Lagrange's porosities among chemo-thermo-poro-mechanics, thermo-poro-mechanics only, and TR only with and without reactive transport.

## CONCLUSIONS

We proposed a sequential implicit formulation and algorithm for chemo-thermo-poro-mechanics, and implemented the coupling algorithm within a flow and geomechanics simulator. This simulator can handle the multiple porosity model in fractured geothermal reservoirs and nonlinear permeability and geomechanics, including plasticity. From numerical simulation of the 2D fractured geothermal reservoir, we found that chemo-thermo-poro-mechanics can yield significantly different results from thermo-poro-mechanics, because small pore volume changes can lead to large fluid pressure effects.

## ACKNOWLEDGMENT

This work was supported by the American Recovery and Reinvestment Act (ARRA), through the Assistant Secretary for Energy Efficiency and Renewable Energy (EERE), Office of Technology Development, Geothermal Technologies Program, of the U.S. Department of Energy under Contract No. DE-AC02-05CH11231, and by 2011 TOUGH2 development grants in the Earth Sciences Division of Lawrence Berkeley National Laboratory.

## REFERENCES

- Barenblatt GE, Zheltov IP, Kochina IN. 1960 Basic concepts in the theory of seepage of homogeneous liquids in fissured rocks. *J. Appl. Math.*;24(5):1286 – 1303.
- Berryman JG. 2002 Extension of poroelastic analysis to double-porosity materials: New technique in microgeomechanics. *J. Eng. Mech.* ASCE; 128(8):840 – 847.
- Johnson J.W., Knauss K.G., Glassley W.E., DeLoach L.D., Tompson A.F.B. 1998. Reactive transport modeling of plug-flow reactor experiments: quartz and tuff dissolution at 240°C. *J. Hydrol* 209:81-111
- Kim J., Sonnenthal E., and Rutqvist J. 2012 Formulation and sequential numerical algorithms of coupled fluid/heat flow and geomechanics for multiple porosity materials. *Int. J. Numer. Meth. Engrg.* doi: 10.1002/nme.4340.
- Kim J. and Moridis G. M. 2012a Gas flow tightly coupled to elastoplastic geomechanics for tight and shale gas reservoirs: material failure and enhanced permeability. *SPE Uncon. Resour. Conf.*, Pittsburgh, PA, 5-7 Jun.
- Kim J. and Moridis G. M. 2012b Numerical Studies for Naturally Fractured Shale Gas Reservoirs: Coupled Flow and Geomechanics in Multiple Porosity/permeability Materials. *46th U.S. Rock Mechanics/Geomechanics Sym.*, Chicago, IL, 24-27 Jun
- Pruess, K., C. Oldenburg, and G. Moridis, 1999 TOUGH2 User's Guide, Version 2.0, Report LBNL-43134, Lawrence Berkeley National Laboratory, Berkeley, Calif.
- Sonnenthal E, Ito A, Spycher N, Yui M, Apps J, Sugita Y, Conrad M, Kawakami S. 2005 Approaches to modeling coupled thermal, hydrological, and chemical processes in the Drift Scale Heater Test at Yucca Mountain. *International Journal of Rock Mechanics and Mining Sciences* 42:698–719.
- Taron J, Elsworth D, Min K. 2009 Numerical simulation of thermo-hydrologic-mechanical-chemical processes in deformable, fractured porous media. *International Journal of Rock Mechanics and Mining Sciences* 46:842–854.
- Wang X. and Wang L.B. and Xu L.M. 2004 Formulation of the return mapping algorithm for elastoplastic soil models. *Comput. Geotech.* 31:315–338.
- Xu T, Sonnenthal E, Spycher N, Pruess K. 2006 TOUGHREACT: A simulation program for non-isothermal multiphase reactive geochemical transport in variably saturated geologic media: Applications to geothermal injectivity and CO2 geological sequestration. *Computers and Geosciences* 32:145–156.
- Xu T, Spycher N, Sonnenthal E, Zhang G, Zheng L, Pruess K. 2011 TOUGHREACT Version 2.0: A simulator for subsurface reactive transport under non-isothermal multiphase flow conditions. *Computers and Geosciences* 37:763–774.